Fast fusion method of virtual image of product shape based on progressive fill line algorithm

Yang Luo

School of Artificial Intelligence,
Chongqing Three Gorges Vocational College,
Wanzhou, Chongqing, 404155, China
Email: 736095906@qq.com

Yan Wang*

School of Academy of Economics and Management,
Chongqing Three Gorges Vocational College,
Wanzhou, Chongqing, 404155, China
Email: yanwa@mls.sinanet.com
*Corresponding author

Abstract: In order to overcome the problems of low precision and speed in the existing fast fusion methods of virtual image of product shape, a new fast fusion method of virtual image of product shape based on progressive fill line algorithm is proposed in this paper. The progressive filling line algorithm is used to fill the virtual image holes of product shape, and dibr technology is introduced to reconstruct the image position and restore the image colour. Finally, the fuzzy minimum error threshold algorithm and Ostu algorithm are used to calculate the optimal threshold and global threshold of the product shape virtual image features, so as to realise the rapid fusion of product shape virtual image. The experimental results show that the design method can ensure the fusion accuracy and clarity of virtual image of product shape, and the shortest fusion time is 7 ms.

Keywords: progressive fill line algorithm; time-varying illumination; product shape; virtual image; image fusion.

Reference to this paper should be made as follows: Luo, Y. and Wang, Y. (2022) 'Fast fusion method of virtual image of product shape based on progressive fill line algorithm', *Int. J. Product Development*, Vol. 26, Nos. 1/2/3/4, pp.143–155.

Biographical notes: Yang Luo, Bachelor of Arts degree, Associate Professor, major of art design, graduated from Chongqing Three Gorges University in 2004, and teaching in Artificial Intelligence Academy of Chongqing Three Gorges Vocational College, the direction of whose is Virtual Reality Technology and Art Design.

Yan Wang, Master degree, a Lecture, graduated from Chongqing Three Gorges University in 2020, majoring in Agricultural Management, teaching in Academy of Economics and Management of Chongqing Three Gorges Vocational College, the direction of whose is Economics and Management and Marketing.

1 Introduction

With the rapid development of modern technology, laser scanning technology appears, which is mainly used in the structure and spatial scanning of machinery and natural geographical environment. Through the generated three-dimensional virtual image, the internal structure of machinery and the spatial structure of environment are demonstrated. However, due to the influence of the level of the equipment itself and external interference factors, the obtained 3D virtual image may be unclear and missing, so a special virtual reconstruction method is needed to make up for the lack of laser scanning (Ueno and Ogawa, 2019). At the same time, due to the interference of light source and other factors, the virtual image of product shape is poor in image quality (Duan et al., 2019), which has attracted extensive attention of relevant scholars. Therefore, it is of great practical significance to study an effective fast fusion method for virtual image of product shape.

In Tsai et al. (2018), a new model of image co saliency detection and co segmentation is proposed, and the concepts of saliency and target in multiple images are studied. The research shows that the common saliency detection by aggregating multiple saliency suggestions from different visual cues can better highlight the saliency target; however, the optimal suggestions are usually region related, and the fusion process often leads to fuzzy results. Its segmentation helps to preserve object boundaries, but it may be affected by complex scenes. In order to solve these problems, we propose a unified method to solve the problem of CO saliency detection and co segmentation by solving the problem of energy minimisation on the graph. This method iteratively performs region adaptive saliency map fusion and target segmentation to transfer useful information between two complementary tasks. Through optimisation iteration and target segmentation, clear saliency mapping is obtained step by step, and the complete saliency target is recovered. At the same time, the segmentation effect is gradually improved due to the improvement of saliency prior knowledge. In Bergstroem et al. (2018), a concept of close range photogrammetry without targets based on computer aided design (CAD) is introduced for online shape detection. Measure the shape of any object on the conveyor belt and compare it with the nominal shape defined by the CAD model. For most manufactured products, the deviation is only measured at a few given comparison points. These deviations can be estimated using local photogrammetry based on prior geometric information given by CAD models and comparison points. Navarro-Alarcon and Liu (2018) describe a method to explore product shape generation in conceptual design phase. The method is based on three concepts: capturing the syntax concept of product appearance, generating sketch conversion rules of design changes, and using parametric modeller to build shape. The product is represented by 3D sketch, which combines the basic shape of simple and schematic product structure. This process allows many different configurations to be created with a minimum of shapes, and helps to generate models for different products.

Although the above methods can achieve image processing or enhancement to some extent, there are some problems such as slow fusion rate and low fusion precision. Therefore, based on the traditional method, aiming at enhancing the effect of product shape virtual image, this paper proposes a fast fusion method of product shape virtual image based on progressive filling line algorithm. The overall research technology of this method is as follows:

1 The progressive filling line algorithm is used to fill the virtual image hole of product shape. According to the algorithm steps, the virtual image of product shape is segmented. Dibr technology is introduced to reconstruct the image position and restore the image colour, so as to improve the effectiveness of the fusion.

2 Based on the above filling results, the best threshold and global threshold of product shape virtual image feature are calculated by using the fuzzy minimum error threshold algorithm and Ostu algorithm, so as to realise the rapid fusion of product shape virtual image.

3 The experimental results show that the convergence, quality and speed of image fusion are used as experimental indexes to compare the method and traditional method.

2 Fast fusion of virtual image of product shape based on progressive fill line algorithm

2.1 Segmentation of virtual image of product shape

In this paper, a fast fusion method of virtual image of product shape based on progressive filling line algorithm is studied. The goal is to fill the occluded virtual image texture into the hole first (Ambron et al., 2020; Alcaide-Marzal et al., 2020). Progressive filling line algorithm is to extract the edge of the product image as the filling line of the remaining holes, and then use the filling line as the search range to find the optimal hole block to fill.

The occluded virtual image of product shape is segmented, that is, the component areas of virtual image of product shape are separated. In this process, the non rigid registration parameters are found by extracting the edge points and the projection contour of the virtual image of the product shape, and then the target area of the image with deformation or disconnection is segmented. In the process of extracting edge points, assuming that the virtual image threshold of product shape is, the calculation result of uniformity measure is as follows:

$$K\left(w\right)=\frac{\alpha^2}{n} \tag{1}$$

In formula (1): α^2 represents the variation value of the segmented region; n represents the non-zero normalisation constant. Using the above calculation to maximise the measurement results, the continuity of edge point extraction is ensured (Cleves et al., 2019; Iwasa et al., 2018; He, 2019). Then, the boundary of the segmented object is extracted, and the local contour feature is extracted by local window

$$C=\sqrt{\frac{\partial K\left(w\right)}{\partial x}+\frac{\partial K\left(w\right)}{\partial y}} \tag{2}$$

In formula (2): C is the local window; x, y is the contour coordinate of the object.

The threshold of gradient image is defined as:

$$E(x,y)=\begin{cases}0 & C<u_2\\ \dfrac{1}{2} & u_1<C\le u_2\\ 1 & C\ge u_1\end{cases} \tag{3}$$

In formula (3): $E(x, y)$ represents the threshold value of gradient image; u_1 and u_2 represents the discrimination coefficient of image pixel value. When the result is 1, the result is boundary; when the result is 0, the result is background. Therefore, the target contour is extracted according to the result.

According to the above operations, the contour segmentation results of the object in the virtual image of the product shape are obtained to form an independent image individual, and then the image position is reconstructed using dibr technology.

2.2 DIBR technology virtual reconstruction image position

DIBR technology is a rendering technology based on depth image. In three-dimensional space, by restoring the basic data of reference image, the information is re projected in the virtual view plane. In this study, according to the image obtained by the above segmentation, its spatial position is calculated, and the image position is reconstructed by dibr technology. The default microlens array is composed of $M\times M$ microlens with 1 focal length and $L\times L$ size. On the optical centre of the middle microlens, the spatial coordinate system is established (Schwein et al., 2018; Li et al., 2019; He et al., 2019; Teodoro et al., 2019). In the space coordinate system which is the origin of A_0 coordinate, the matching points of the upper and lower images are obtained, which are $P_1(x_1, y_1, z_1)$ and $P_2(x_2, y_2, z_2)$ respectively.

According to the transformation relationship between 3D space points and corresponding imaging plane points, the coordinates of space point $X(x_w, y_w, z_w)$ are as follows:

$$I_A = M, X = x_w, Y = y_w, Z = z_w \tag{4}$$

Through the above calculation process, the position virtual reconstruction of the segmented image is realised (Xin et al., 2018). After the virtual reconstruction of the position, the colour of the virtual image of the product shape is restored.

The colour of the virtual image of the known product shape is related to the characteristics of the microlens, the photosensitive equipment, the length of the incident light wave and the attenuation degree of the light intensity in the air. Therefore, it is necessary to reconstruct the reflected light wavelength of the space point, and calculate the attenuation of the reflected light in the air through the relative position information of the space point and the microlens. Combined with the characteristics of the microlens, the generated colour of the incident light on the photosensitive element is calculated, so as to realise the colour recovery of the segmented image (Wei, 2019). The position of the virtual image of the product shape is known, and the lens parameters in the previous section are the basic conditions. The projection position of the space point in the micro transparent mirror is calculated by using the geometric model. According to the

definition of image colour, the virtual image colour after virtual reconstruction is calculated. Therefore, it is assumed that the appearance of the virtual object in the three-dimensional image is Lambert surface, and the pixel colour obtained by laser scanning at a certain time is:

$$s_{i,j}(x,y) = I_A\left[\mu, H(\beta, c, \mu), \gamma\right] \tag{5}$$

In formula (5): $s_{i,j}(x,y)$ represents the pixel colour of the occluded object in the virtual image of the product shape; μ represents the wavelength of the incident light; H represents the air attenuation factor; β represents the angle of light incidence; c represents the distance from the light source; γ represents the characteristics of the microlens (Wegener et al., 2018).

Given that γ is fixed, we need to consider the matching points in the image, the position and colour in the virtual reconstruction process. Because the points in the space corresponding to the left, middle and right images are the same, the incident light wavelength μ is fixed by default. According to the matching points of the left and right images, the space points are calculated through the geometric relationship. According to the positions of the space points and the middle microlens, the β and c values in the formula are calculated.

$$\beta = acc\cot\left(X_w \big/ H\right) \tag{6}$$

As c value represents the distance of light source, it cannot be described by analytical formula alone. Therefore, artificial neural network is used for data sampling. The sampling diagram of artificial neural network is shown in Figure 1 (Teodoro et al., 2019).

Figure 1 A sample diagram of an artificial neural network

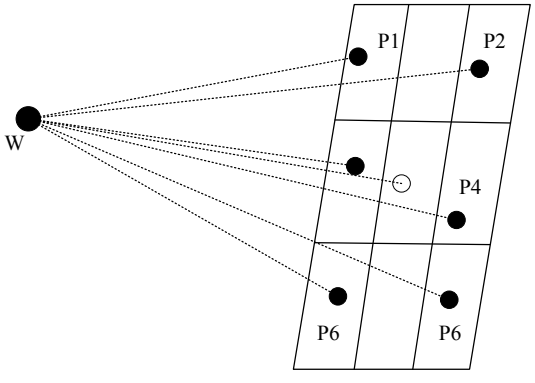

Through the above sampling, the value of light source distance c is determined to complete the colour restoration of product shape virtual image segmentation by DIBR technology. Before image fusion, fuzzy minimum error thresholding algorithm and Ostu algorithm are used to calculate the optimal threshold and global threshold of image features, determine fusion parameters (Huang and Manh, 2018), and fuse range image and intensity image according to fusion rules.

2.3 Fast fusion of virtual image of product shape

Fuzzy minimum error threshold algorithm is used to separate the pixel gray mutation points of the identified image features according to noise points and edge points. Let the pixel gray mutation point be t, t_1 denote the noise point area segmented from it, and its membership function be $\theta_1 = (b, e, n)$; t_2 denote the edge point area segmented from it, and its membership function be $\theta_2 = (b, e, n)$. the above two membership functions can describe the membership degree of t_1 and t_2 to the image feature b, that is, the probability that the pixel corresponding to the image feature is determined to be edge point and noise point. Where (e, n) is a given parameter, and t is divided into edge point region and noise point region by these two parameters. Suppose $t_1 \sim R\left[s_1(e,n), \rho_1^2(e,n)\right]$ and $t_2 \sim R\left[s_2(e,n), \rho_2^2(e,n)\right]$, then the pixels of edge points and noise points in t are:

$$\begin{aligned} v_c = & \frac{w_1}{\sqrt{\pi}\rho_1^2(e,n)} \exp\left(\sum s_1 \Big/ \rho_1\right) \\ & + \frac{w_2}{\sqrt{\pi}\rho_2^2(e,n)} \exp\left(\int s_2 \Big/ \rho_2 \, d\rho\right) \end{aligned} \tag{7}$$

Formula (9), formula (10) and formula (11) represent variance $\rho_i^2(e,n)$, noise probability $r_i(e,n)$ and mean value $f_i(e,n)$ corresponding to formula (8) respectively

$$\rho_i^2(e,n) = \sum_{b=1}^{k} \left[b - f_i(e,n)\right] \rho_i^2(e,n) v_c \tag{8}$$

$$r_i(e,n) = \int_{i=1}^{k} \rho_i^2(e,n) v_c db \tag{9}$$

$$f_i(e,n) = \frac{\sum_{b=1}^{k} \left[b - f_i(e,n)\right] v_c}{r_i(e,n)} \tag{10}$$

In formula (9), formula (10) and formula (11): k represents the number of image features. On this basis, the error function $G(e, n)$ is defined as:

$$G(e,n) = \ln \rho_i^2(e,n) + w r_i(e,n) \tag{11}$$

In order to get the best threshold of image, we need to find the parameter (e, n), which corresponds to the minimum classification error

$$(e,n) = \arg\max\left[G(e,n)\right] \tag{12}$$

In order to obtain the optimal threshold, formula (12) needs to be brought into the minimum error formula to obtain the optimal parameter (e_{new}, n_{new}). X_{new} represents the optimal threshold (Lian et al., 2018).

$$X_{new} = \frac{\pi\left(e_{new} + n_{new}\right)}{2} \tag{13}$$

On the basis of the steps, the gradient value and intra group variance of Sobel operator are calculated by formula (14) and formula (15):

$$B(i,j) = X_{new}\sqrt{i^2 + j^2} \tag{14}$$

$$\delta = \rho_1^2\omega_1(b) + \rho_2^2\omega_2(b) \tag{15}$$

Where ω represents Sobel operator, i represents gradient value in horizontal direction, j represents gradient value in vertical direction, and gradient image $B(i, j)$ is composed of gradient values of all pixels. The global threshold D of the whole image feature is calculated by Ostu algorithm, and the image feature is divided into gray mutation region and gray flat region according to the global threshold. Suppose that the gray level of the original image corresponding to D is divided into two groups V_1 and V_2, which correspond to the region with small gray value change and the region with large gray value change respectively. In this case, the variance between groups is the largest and the variance within groups is the smallest.

$$\rho_i^2(b) = \omega_1\omega_2(b) \Big/ \sum_{b=1}\left[V_1(b) - V_2(b)\right] \tag{16}$$

Ostu algorithm is considered from the perspective of global gray distribution, and is the key part of image feature separation.

In practical applications, speckle noise will affect the range profile and intensity profile of image features. There are differences between the intensity image and the distance image. In order to determine whether the pixels in the distance image belong to the edge region or the signal region, it is necessary to determine the gradient value, while the intensity image will produce gray continuity only in the homogeneous region (Song et al., 2019).

Use the above method to calculate the threshold D_3 and threshold D_4 of the distance gradient image. If there is a point with a maximum gradient value, then this point must be an edge point, and D_4 is the threshold value of the decision. If there is a point whose gradient value is less than the global threshold D_3, it is judged that the point is a noise point. There is local standard deviation of intensity image between D_1 and D_2, and there is gradient value in distance image between D_3 and D_4. In order to divide pixels into different regions, there is no need to deal with the pixels of edge points and signal points, only different thresholds are selected. The mean value of 8 pixels in the neighbourhood is used to replace the noise points

$$D = \begin{cases} D_1[0, D_1] \\ D_2[D_1, D_2] \cap [D_4, +\infty] \\ D_3[D_1, D_2] \cap [D_3, D_4] \\ D_4[D_2, +\infty) \end{cases} \tag{17}$$

Middle point fusion rule: the optimal threshold of intensity gradient graph is D_5, the middle point less than D_5 is the edge point, and the middle point greater than D_5 is the noise point.

Through the above calculation, the rapid fusion of virtual image of product shape is completed, and the overall quality of virtual image design of product shape is improved. Next, the performance of the proposed method is verified by simulation experiments.

3 Simulation experiment

In order to analyse the image fusion effect of this method, a total of 500 groups of 1000 virtual images of product appearance are selected, including 370 beauty images, 100 food images, 120 clothing images, 110 electrical images, 120 PET images and 180 home decoration images. The detailed description of the target sample distribution of each image is shown in Table 1.

Table 1 Target sample distribution

Image category	*Test sample*	*Training sample*	*Total number of samples*
Beauty image	260	110	370
Food image	70	30	100
Clothing image	86	34	120
Electrical image	58	42	110
PET image	64	56	120
Home decoration image	93	87	180

Based on the above experimental data, comparative verification experiments were carried out. The overall experimental scheme is set as follows: taking image fusion convergence, image fusion quality and image fusion speed as experimental comparison indexes, the method in this paper is compared with Tsai et al. (2018), Bergstroem et al. (2018) and Navarro-Alarcon and Liu (2018). The method of this study was taken as the experimental group, and the method based on Collaborative segmentation in Tsai et al. (2018), the method based on aimless CAD in Bergstroem et al. (2018) and the method based on 3D modelling in Navarro-Alarcon and Liu (2018) were taken as control group A, control group B and control group C respectively.

3.1 Convergence comparison of image fusion

The convergence comparison results of the four methods are shown in Figure 2.

It can be seen from the comparison results in Figure 2 that the convergence of this method is always better than the three literature comparison methods in the three convergence comparison test results.

Figure 2 Convergence test results of fused images

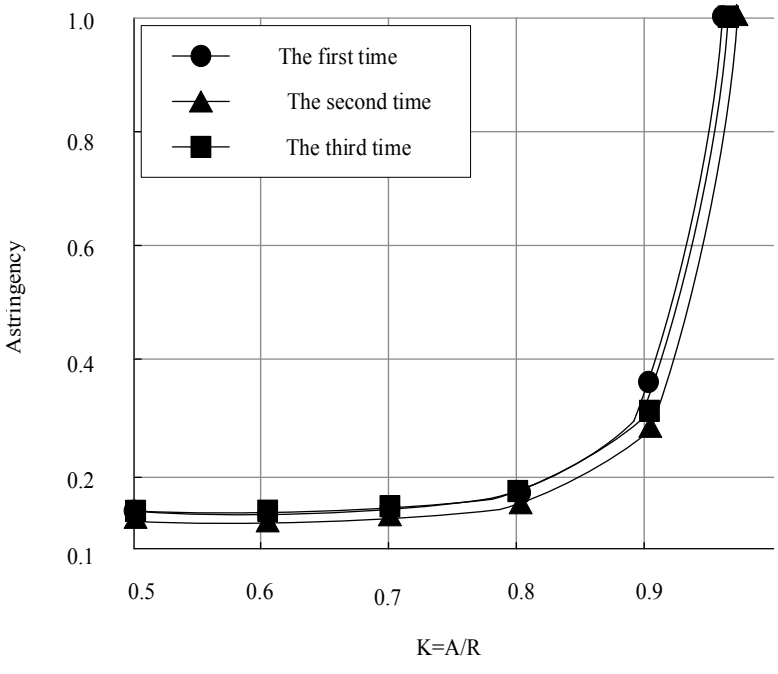

(a) Experimental group test results

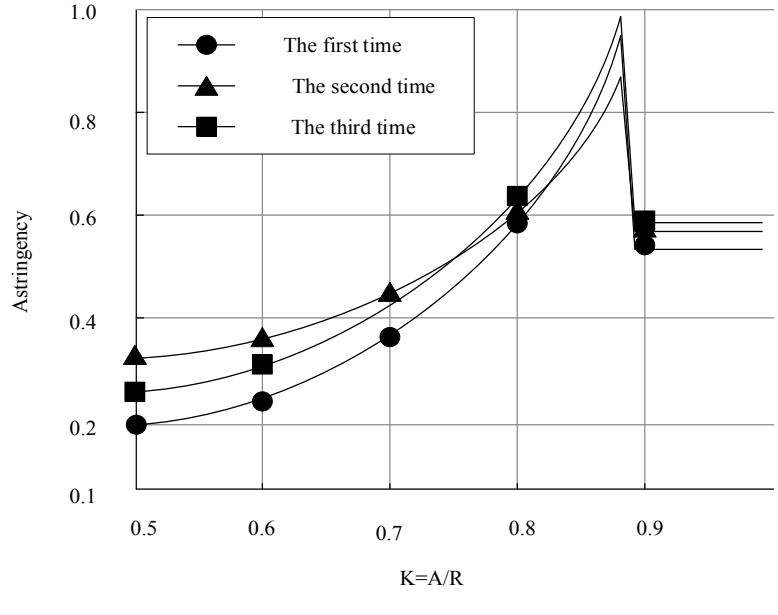

(b) Results of A control group

Figure 2 Convergence test results of fused images (continued)

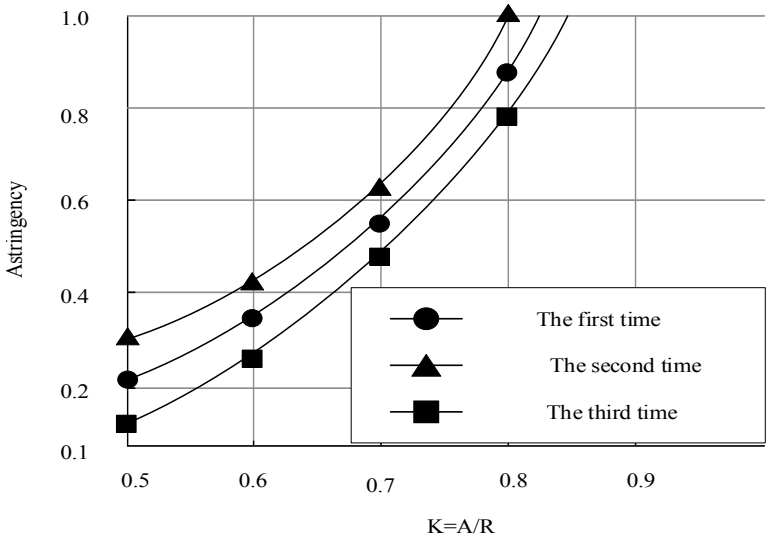

(c) Results of B control group

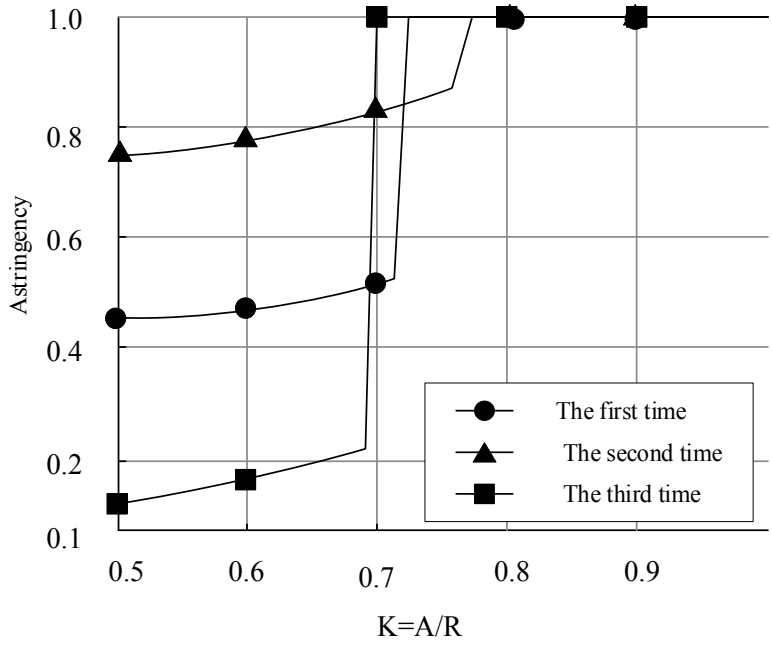

(d) Results of C control group

3.2 Image fusion quality comparison

In order to ensure the accuracy of the test results, each test group conducted a total of three experiments. The quality evaluation results of the three methods are shown in Table 2.

Table 2 Fusion quality evaluation

Evaluating indicator	*Control group A*	*Control group B*	*Control group C*	*Experimental group*
Root mean square error	0.3265	0.4952	0.2758	0.1025
Average gradient	0.1263	0.3698	0.4578	0.0518
Information entropy	7.1591	6.9581	5.674	10.5102
Mean value	0.5961	0.7923	0.8781	0.2317
Spatial frequency	16.597	15.6974	15.6449	26.1929
Definition	0.5963	0.8721	0.5678	1.3697

It can be seen from Table 2 that compared with the other two methods, the average gradient, information entropy and clarity of the fused image of this method are higher, while the root mean square error is lower, and the average value is moderate, which proves that the virtual image of product shape fused by this method has good clarity and brightness. From the perspective of spatial frequency, the spatial frequency of this method is the highest, which proves that the virtual image of product shape fused by this method maintains a good degree of spatial activity, and the fused virtual image of product shape is better.

3.3 Image fusion speed comparison

Finally, the image fusion speed is tested in groups. Figure 3 shows the fusion speed test results of 1000 sample images in four test groups.

Figure 3 Image fusion speed test results

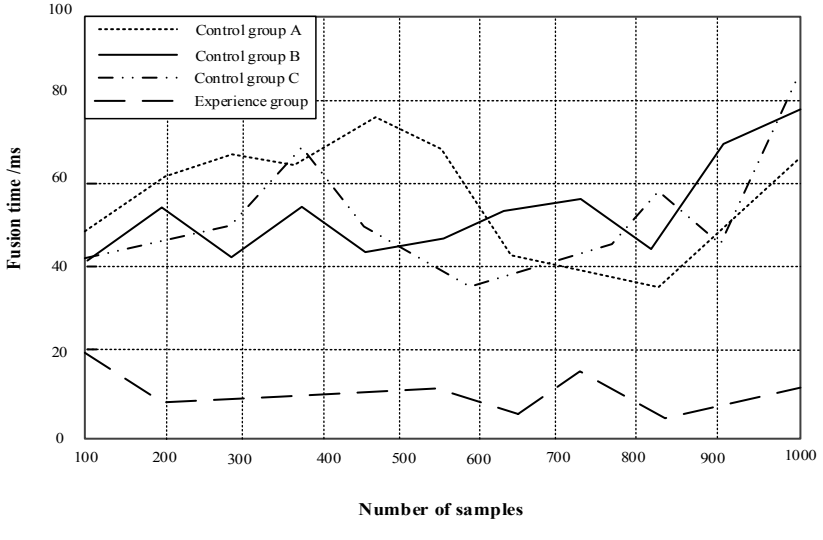

The image fusion speed of the four test groups was compared, and it was found that the image fusion speed of the experimental group was lower than that of the three control groups, which was within 20 ms. Because the image fusion time is within 20 ms, it can be seen that the research based on progressive filling line algorithm for product shape virtual image fusion method, on the basis of ensuring the image fusion quality, has accelerated the image fusion speed to the maximum extent.

4 Conclusion

In order to improve the effectiveness of fast fusion of virtual image of product shape, a fast fusion method of virtual image of product shape based on progressive fill line algorithm is proposed. The performance of the method is verified from both theoretical and experimental aspects. This method has high fusion quality and speed in fast fusion of virtual image of product shape. Specifically, compared with the method based on Collaborative segmentation, the fusion quality is significantly improved, and the fusion clarity reaches 1.3697; compared with the method based on non target CAD, the fusion speed is greatly improved, and the maximum fusion time is less than 20ms. Therefore, it fully shows that the proposed fusion method based on progressive fill line algorithm can better meet the requirements of product shape virtual image fast fusion. In the future research work, we should further improve the quality of virtual image fusion to improve the reliability of product shape design.

Acknowledgements

This paper was supported by 2021 Humanities and Social Science Research Project of Chongqing Education Commission: 'Research on Digital Protection and Inheritance of the Three Gorges Civil Stone Jars Based on Virtual Reality (VR) Design' (Project No. 21SKGH358).

References

Alcaide-Marzal, J., Diego-Mas, J.A. and Acosta-Zazueta, G. (2020) 'A 3D shape generative method for aesthetic product design', *Design Studies*, Vol. 66, No. 35, pp.144–176.

Ambron, E., Miller, A., Connor, S. and Coslett, H.B. (2020) 'Virtual image of a hand displaced in space influences action performance of the real hand', *Scientific Reports*, Vol. 10, No. 1, 9515.

Bergstroem, P., Fergusson, M. and Sjoedahl, M. (2018) 'Virtual projective shape matching in targetless CAD-based close-range photogrammetry for efficient estimation of specific deviations', *Optical Engineering*, Vol. 57, No. 5, pp.531–538.

Cleves, A.E., Johnson, S.R. and Jain, A.N. (2019) 'Electrostatic-field and surface-shape similarity for virtual screening and pose prediction', *J Comput Aided Mol Des.*, Vol. 33, No. 10, pp.865–886.

Duan, J., Xiao, S., Zhang, K. and Jing, Y. (2019) 'A novel 3-D analytical modeling method of trapezoidal shape permanent magnet halbach array for multi-objective optimization', *Journal of Electrical Engineering and Technology*, Vol. 14, No. 2, pp.635–643.

He, G., Xing, S., He, X., Wang, J. and Fan, J. (2019) 'Image fusion method based on simultaneous sparse representation with non-subsampled contourlet transform', *IET Computer Vision*, Vol. 13, No. 2, pp.240–248.

He, J. (2019) 'Digital image progressive fusion simulation in decoupling cascaded complex networks', *Computer Simulation*, Vol. 36, No. 11, pp.370–373+382.

Huang, C.C. and Manh, H.N. (2018) 'X-ray enhancement based on component attenuation, contrast adjustment, and image fusion', *IEEE Transactions on Image Processing*, Vol. 16, No. 8, pp.1–10.

Iwasa, T., Ota, K., Harada, T. and Muramatsu, R. (2018) 'High-resolution surface shape measurement of parabola antenna reflector by using grating projection method with virtual targets', *Acta Astronautica*, Vol. 15, No. 3, pp.95–108.

Li, H., Zhang, X. and Miao, W. (2019) 'Multiple target information fusion matching algorithm based on a line laser and a single plane array camera', *Applied Optics*, Vol. 58, No. 15, pp.4025–4035.

Lian, C., Ruan, S., Denux, T., Li, H. and Vera, P. (2018) 'Joint tumor segmentation in PET-CT images using co-clustering and fusion based on belief functions', *IEEE Transactions on Image Processing*, Vol. 28, No. 2, pp.755–766.

Navarro-Alarcon, D. and Liu, Y.H. (2018) 'Fourier-based shape servoing: a new feedback method to actively deform soft objects into desired 2-D image contours', *IEEE Transactions on Robotics*, Vol. 25, No. 9, pp.1–8.

Schwein, A., Chinnadurai, P., Behler, G., Lumsden, A.B., Bismuth, J. and Bechara, C.F. (2018) 'Computed tomography angiography-fluoroscopy image fusion allows visceral vessel cannulation without angiography during fenestrated endovascular aneurysm repair', *Journal of Vascular Surgery*, Vol. 35, No. 6, pp.163–169.

Song, J., Shi, Z., Du, B., Han, L., Wang, Z. and Wang, H. (2019) 'The data fusion method of redundant gyroscope system based on virtual gyroscope technology', *IEEE Sensors Journal*, Vol. 19, No. 22, pp.10736–10743.

Teodoro, A.M., Bioucas-Dias, J.M. and Figueiredo, M.A.T. (2019) 'A convergent image fusion algorithm using scene-adapted Gaussian-mixture-based denoising', *IEEE Transactions on Image Processing*, Vol. 28, No. 1, pp.451–463.

Tsai, C.C., Li, W., Hsu, K.J., Qian, X. and Lin, Y.Y. (2018) 'Image co-saliency detection and co-segmentation via progressive joint optimization', *IEEE Transactions on Image Processing*, Vol. 28, No. 1, pp.56–71.

Ueno, A. and Ogawa, Y. (2019) 'Influence of coarse aggregate shape on optimum fine to total aggregate ratio using a virtual voids-ratio diagram in concrete compaction', *Cement and Concrete Composites*, Vol. 10, No. 6, pp.103–108.

Wegener, D., Zips, D., Thorwarth, D. et al. (2018) 'Precision of MR-CT image fusion based on gold markers for the prostate cancer IGRT under usage of a phantom and clinical data', *Strahlentherapie und Onkologie*, Vol. 194, No. 11, pp.S161–S162.

Wei, Y. (2019) 'Three-dimensional laser image-filtering algorithm based on multi-source information fusion and adaptive offline fog computing', *Multimedia Systems*, Vol. 26, No. 1, pp.17–26.

Xin, J., Qian, J., Zhou, D. and Nie, R. (2018) 'Infrared and visual image fusion method based on discrete cosine transform and local spatial frequency in discrete stationary wavelet transform domain', *Infrared Physics & Technology*, Vol. 26, No. 7, pp.234–140.